scientific reports

OPEN

The influence of Sn particle incorporation on the photocatalytic activity of sprayed ZnO–SnO$_2$ nanocomposites

S. Mahjoubi[1], M. Mezyen[1], G. El Fidha[1,2], N. Bitri[1✉] & E. Llobet[3✉]

This paper investigates the photocatalytic performance of ZnO–SnO$_2$ nanocomposites deposited using the Spray Pyrolysis technique, with varying percentages of tin oxide (20, 60, and 80%) on glass substrates at 350 °C. Comprehensive characterization of the samples was carried out using X-ray diffraction (XRD), Scanning Electron Microscopy (SEM), Atomic Force Microscopy (AFM), and UV–Vis spectroscopy to analyze their structural, morphological, and optical properties. The XRD analysis confirmed the hexagonal structure of zinc oxide and the tetragonal phase of tin oxide in the nanocomposites. The average crystallite size was found to decrease with an increase in the percentage of tin oxide. The UV–Vis spectra demonstrated that the band gap energy of the ZnO–SnO$_2$ nanocomposite increased from 3.29 to 3.64 eV as the amount of Sn increased. The Urbach energy decreases reflecting an improvement in the structural and electronic quality of the material, with fewer defects and better crystallinity. Additionally, The SEM results reveal a transition in surface morphology with increasing Sn content, shifting from a smooth, compact structure to a highly aggregated particle surface, with the highest thickness (740 nm) observed at 80% SnO$_2$. Remarkably, the ZnO–SnO$_2$ nanocomposite with 80% tin exhibited superior photocatalytic activity, successfully degrading 91% of methylene blue solution within 180 min under UV irradiation. Moreover, the stability and reusability of the sample were demonstrated through repeated photocatalytic cycles. The use of a chemical synthesis technique for the elaboration of the Sn:Zn mixed nanocomposite and UV light as catalyzer which, is well suited for large bandgap materials, optimizes this work by providing an increased contact surface area and facilitating the interaction between the photocatalyst and the target molecules. These findings highlight its potential for effective environmental applications, specifically in photocatalysis for pollution control and environmental protection. The results collectively suggest that ZnO–SnO$_2$ nanocomposites, deposited through the spray method, represent promising candidates for advancing photocatalytic technologies.

Keywords ZnO–SnO$_2$, Spray, Photocatalysis, Nanocomposites, Methylene blue

The present-day requirements for technology aligning with the seamless transmission of environmental data, especially within the framework of the Internet of Things (IoT), are driving continuous progress in various integral electronic components. These include, but are not limited to photocatalysts[1], gas sensors[2], solar cells[3], and optoelectronic devices[4], reflecting a dynamic landscape of innovations aimed at enhancing our ability to monitor and respond to environmental challenges.

All of these cutting-edge devices intricately depend on the fundamental functionality of semiconductor materials, where transparent conductive materials play a pivotal role. These materials are characterized by high transmittance in the ultraviolet–visible (UV–Vis) wavelength range and electrical conductivity[5].

Among transparent conductive oxides (TCO), Zinc Oxide (ZnO) shows promise for the degradation of dye pollutants in photocatalytic treatment due to its non-toxic characteristics, high stability, low cost, a direct band gap of 3.36 eV, and n-type material properties, allowing it to tune with other elements for better catalytic and optoelectronic properties[6,7].

[1]Laboratoire de Photovoltaïque et Matériaux semi-conducteurs, Université de Tunis El Manar, Ecole Nationale d'Ingénieurs de Tunis, 1002 Tunis, Tunisia. [2]Université de Tunis, Ecole Nationale Supérieure d'ingénieurs de Tunis, Avenue Taha Hussein Montfleury, 1008 Tunis, Tunisia. [3]Universitat Rovira i Virgili, ETSE, Avda. Països Catalans, 26, 43007 Tarragona, Spain. ✉email: nabila.bitri@enit.utm.tn; eduard.llobet@urv.cat

A key research concern involves the elimination of hazardous dyes extensively employed as coloring agents in various industries such as textiles, leather, food, plastics, and cosmetics[8]. However, a significant drawback is that the majority of industrial dyes exhibit toxicity, carcinogenicity, and mutagenicity, coupled with low biodegradability[9]. Health risks associated with some synthetic dyes include allergic reactions and skin irritations. Additionally, the persistence of certain dyes in the environment contributes to long-term pollution, and their limited biodegradability poses disposal challenges. Effluents containing these dyes are highly pigmented, and releasing them into natural water bodies can disrupt aquatic ecosystems by impeding sunlight penetration, leading to a decline in dissolved oxygen levels[10]. Hence, the removal of dyes before discharging wastewater from dye industries is crucial for preserving environmental balance.

The degradation of dyes involves various techniques aimed at breaking down or transforming dye molecules into less harmful substances. Adsorption plays an important role in environmental remediation by facilitating the accumulation of pollutants on the surface of materials. It is widely valued for its simplicity, affordability, and efficiency in capturing a variety of contaminants, including both organic and inorganic substances. On the other hand, Advanced Oxidation Processes (AOPs) have emerged as potent methods for breaking down organic pollutants[11]. These processes work by generating reactive species, such as hydroxyl radicals (OH·), which can react quickly with all organic electron-rich molecules, breaking down harmful substances into less hazardous byproducts[12,13]. A combined approach involving adsorption and AOPs has shown great promise, as the adsorption step helps concentrate pollutants on the catalyst surface, enhancing their subsequent breakdown through oxidation[14]. Advanced Oxidation Processes (AOPs) involve many techniques, such as photocatalysis, that utilize reactive species like hydroxyl radicals to oxidize and degrade dyes. Biological methods employ microorganisms, enzymes, or fungi to metabolize and break down dyes into simpler components. Adsorption onto activated carbon or other adsorbents can effectively remove dyes from water, although this is not a true degradation process. Electrochemical degradation, involving the use of electrodes and applied electric potential, has also shown promise in breaking down dye molecules[15]. The choice of technique often depends on the specific dye type, environmental conditions, and the desired level of treatment efficiency.

The photocatalysis technique offers several advantageous features, including its low-cost nature. The process relies on abundant and affordable materials, such as titanium dioxide, reducing overall implementation expenses. Additionally, its energy efficiency, driven by natural or artificial light sources, contributes to cost-effectiveness. Moreover, the technique's versatility makes it suitable for various applications, providing an economically viable and sustainable solution for pollution control and environmental remediation. Despite its significant advantages, this technique is still facing some challenges, like electron-hole recombination and low light absorption, that can be addressed by doping, use of nanostructured materials, and the design of hybrid systems to enhance efficiency. For example, D.Pathania et al. succeeded in reaching a photocatalytic efficacy of around 91.8% for the degradation of methylene blue (MB) under sunlight for 3 h using gold nanoparticles (AuNPs) supported by Cymbopogon flexuosus essential oil for their elaboration[16].

The photocatalysis of water was first described and discovered in 1972 by Fujishima and Honda[17]. The principle can be elucidated as follows: When a photocatalyst is illuminated with light energy equal to or higher than its band gap energy, electron/hole pairs (e^-/h^+) are generated. These photogenerated charge carriers migrate to the surface of the photocatalyst, where they interact with adsorbed species, such as water molecules and oxygen. Highly reactive radicals like hydroxyl radicals (·OH) and superoxide radicals (O_2·$^-$) are created when these photogenerated charge carriers move to the catalyst's surface and interact with adsorbed species. The oxidation of organic pollutants into less hazardous byproducts like CO_2 and H_2O is largely dependent on these radicals[18].

In an aqueous or gaseous medium, reactants can adsorb onto the photocatalyst surface and undergo direct or indirect reactions with the photogenerated electrons and holes[19]. However, the efficiency of water purification from waste depends on factors such as the surface area of the photocatalyst and the energy of the electron-hole pairs produced, as well as the extent of their separation[20,21]. D. Pathania et al. synthesized magnesium nanoparticles (MgNPs) and noticed that samples showing smaller particle size exhibited better photocatalytic efficiency (91.2%) in degrading MB under direct sunlight radiation for 3 h[22]. Several studies have reported the effective use of photocatalysis to break down organic dyes and other contaminants when exposed to UV and solar radiation by manipulating the key factors of this process. For instance, recent studies carried out by I. Ameur et al. proved that elevating crystallinity, roughness and gap energy levels by doping Mg into the ZnO thin film structures can improve the photocatalytic stability and activity[23]. Similarly, because of their large surface area (porous surface) and effective charge carrier dynamics, the SnO_2/TiO_2-50 heterostructures elaborated by S.Kimet et al. have demonstrated encouraging outcomes (99% degradation efficiency with a high kinetic constant of 0.013 min^{-1}) in using solar radiation for MB degradation[24]. These results emphasize how crucial material optimization and design are to attaining effective photocatalytic performance.

TCO configurations have been purposefully crafted to enhance the characteristics of Transparent Conductive Oxides for application in photocatalysis, as outlined in prior works[7,25,26]. A full study has been carried out by A. Kulis-Kapuscinska et al. on porous ZnO thin films achieving 64% MB removal for 540 min. Actually, their study was based on a deep analysis of the degradation mechanism by exploring the SEM and XPS data before and after the photodegradation process, proving the sustainability and reproducibility of the ZnO sputtered thin films[27]. The Recent research efforts advocate for the synergistic integration of ZnO with other semiconductors. Researchers have underscored that such combinations represent a promising strategy for mitigating the recombination rate of charge carriers[28]. This approach not only amplifies the charge separation efficiency of conventional photocatalysts[29] but also holds potential for advancing the mineralization of toxic organic pollutant dyes[30].

Various composite forms involving ZnO have been suggested, including ZnO–TiO_2[31], ZnO–CdS[32,33], ZnO–AgBr[34], ZnO–Ag_2S[35], and ZnO–SnO_2[36,37]. Notably, among these configurations, the ZnO–SnO_2 nanocomposite

stands out as an exceptional material due to its remarkably high photocatalytic activity, as corroborated by recent studies[36,38–41].

This heterojunction nanomaterial demonstrates remarkable degradation efficiency for a wide range of dyes, displaying its potential in environmental remediation. Notably, S. Begum et al. successfully synthesized a ZnO–SnO$_2$ nanocomposite via the co-precipitation method, which exhibited an impressive ability to degrade 97% of Biebrich Scarlet dye (10 mg/L) within just 40 min under UV light irradiation. Furthermore, the material demonstrated excellent reusability, maintaining its catalytic performance over eight consecutive cycles[42]. MB and Chromium (VI) were used as model dyes by D. Venkatesh et al. to evaluate the degradation efficiency of the ZnO–SnO$_2$ nanocomposite. Their study demonstrated impressive results, achieving degradation rates of 89% for MB and 92% for Chromium (VI) within 90 min of solar light exposure[43].

In this study, we introduce a novel approach to enhancing the photocatalytic properties of ZnO–SnO$_2$ nanocomposites by systematically varying the percentage of Sn deposited using spray pyrolysis. Unlike previous works that have primarily focused on fixed compositions of ZnO–SnO$_2$, our method allows for the precise control of Sn content, enabling us to investigate its impact on photocatalytic activity. By leveraging the advantages of spray pyrolysis, which yields porous thin films conducive to enhanced dye adsorption and reaction kinetics, we optimize the contact surface area between the photocatalyst and the dye molecules, facilitating faster and more efficient photocatalytic reactions.

Different techniques have been used to prepare ZnO–SnO$_2$ nanocomposites, such as hydrothermal methods[44], sol-gel[45,46], co-precipitation[47], and atomic layer deposition[48–50]. In this paper, ZnO–SnO$_2$ nanocomposites were meticulously deposited by spray pyrolysis, varying the volume percentages of Sn (Zn:Sn of 100:0%, 80:20%, 50:50%, 20:80%, and 0:100%). The combination between ZnO and SnO$_2$ is chosen for its complementary properties, where ZnO offers high photocatalytic activity, and SnO$_2$ enhances stability and charge separation. Their synergistic heterojunction improves light absorption, electron-hole separation, and pollutant degradation efficiency. Our main objective in this study is to elucidate the impact of the incorporation of the Sn element on the photocatalytic activity.

Experimental details
Preparation of ZnO–SnO$_2$ thin films
Pure oxides of ZnO and SnO$_2$ and the nanocomposites of ZnO–SnO$_2$ (Z:S) with different percentage of tin oxide 20, 50 and 80%, were deposited by chemical spray pyrolysis onto glass substrates at 350 °C.

Glass substrates were cleaned using ethanol, acetone, hydrochloric acid (HCl) and distilled water and werethen dried in a furnace at 120 °C for 15 min.

Zinc chloride (ZnCl$_2$· 2H$_2$O, Sigma Aldrich >%99) and tin chloride (SnCl$_2$·2H$_2$O, Sigma Aldrich >%99) were used to prepare the different samples.

The spray solution was prepared by dissolving 0.05 M of zinc chloride and 0.05 M of tin chloride in 200 mL of distilled water independently and was sprayed at the rate of 2 mL/min. All variables were carefully managed during the experiment. This included maintaining a consistent flow of 10 mL·min^{-1} for the air compression carrying gas and controlling substrate temperatures at 350 °C. Temperature regulation was achieved using a thermocouple connected to the hotplate where the substrates were situated. Furthermore, the distance between the nozzle and the substrates was estimated to be 20 cm.

SnO$_2$ solution was added to the ZnO precursor solution at different volume percentages, such as 20, 50, and 80%. The elaboration process is represented and detailed in Fig. 1.

Characterization of Zn:SnO$_2$ thin films
The microstructure of the films was studied at room temperature by high-resolution X-ray diffraction (XRD, X'pert PRO, Philips) with monochromatic CuKα radiation (λ = 1.541874 Å) at 40 kV and 30 mA in θ–2θ configuration from 10 to 70° with a step of 0.05°.

The surface morphology was analyzed by Atomic Force Microscopy (AFM) and Electron scanning microscopy (SEM) using a commercial microscope (Bruker, MultiMode) and HITACHI-S4800, respectively, in ambient conditions. The optical transmittance was recorded from 300 to 1800 nm using UV–Vis spectrophotometer Shimadzu UV 3100 S double beam spectrophotometer. The optical properties were studied to determine the optical parameters such as the transmittance, the band gap energy and the Urbach energy.

Photocatalytic experiment
The photocatalytic activity of ZnO–SnO$_2$ nanocomposites with different percentages of tin oxides, was evaluated by a photoreactor using a 100 W UV–C lamp.

For the measurement of the photocatalytic activity, (MB) was chosen as an organic pollutant. The evaluation of the degradation of the MB was studied using a Shimadzu-UV1800 spectrophotometer. The absorption was monitored in the wavelength range of 300–800 nm, showing a decrease in the peak intensity at 660 nm.

The degradation under Ultraviolet light irradiation for ZnO–SnO$_2$ nanocomposites was studied. An aqueous solution of MB with a concentration of 3 mg L^{-1} was stirred for a few minutes. Afterwards, thin films of pure oxides (pure zinc and pure tin) and ZnO–SnO$_2$ nanocomposites (20%, 50% and 80%) were placed into 5 glass boxes containing 30 mL of MB solution and were magnetically stirred and kept under dark conditions for 30 min. Then, they were exposed to Ultraviolet radiation for different times: 30, 60, 120 and 180 min.
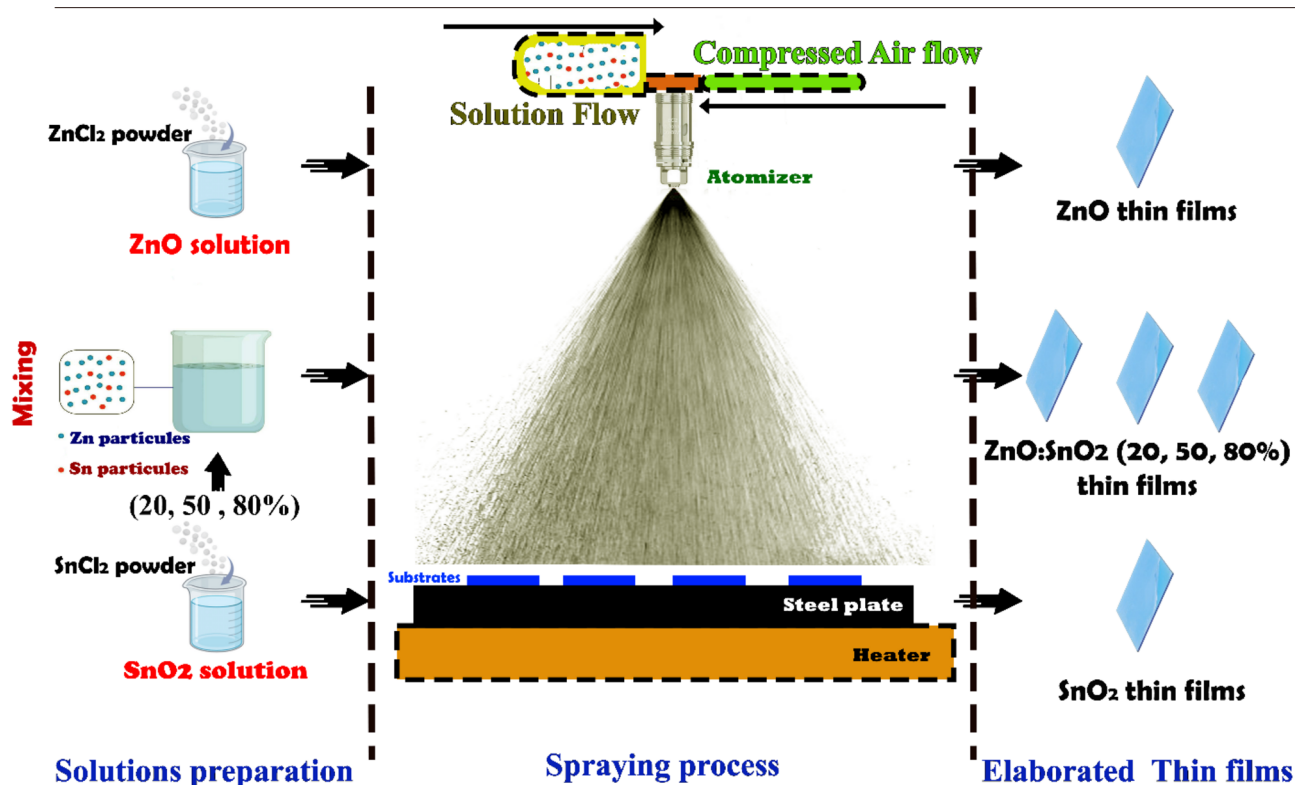
Fig. 1. Schematic representation of spray pyrolysis process for ZnO, SnO$_2$ and ZnO−SnO$_2$ thin film deposition.

Results and discussion
Structural and morphological properties

In order to investigate the crystalline quality of the films ZnO−SnO$_2$ with various percentages of SnO$_2$, XRD analysis was carried out. X-ray diffractograms of pure ZnO, pure SnO$_2$ and ZnO−SnO$_2$ sprayed with different percentages of SnO$_2$ (20, 50 and 80%) are shown in Fig. 2.

For pure oxides, pure ZnO and pure SnO$_2$, we can see only the peaks assigned to the hexagonal structure of zinc oxide and the tetragonal phase of tin oxide according to JCPDS card Nos. (080−0074) and (001−0657), respectively. The diffraction peaks of the samples are sharp and intense, and no other phases were found in the films, confirming their high purity and crystallinity.

For the samples prepared with 20 and 50% SnO$_2$, the predominance of the ZnO phase is evident, while tin oxide is only minimally observed, indicated by the presence of the (310) peak, which suggests that for these percentages, the SnO$_2$ is present in an amorphous phase. Furthermore, a decrease in the intensity of the preferential peak of ZnO (002) is noteworthy.

By increasing the percentage of SnO$_2$ from 50 to 80%, we notice the appearance of the peaks assigned to the SnO$_2$ phase with a tetragonal structure, such as (110), (200) and (211), whereas the intensity of the preferential peak for ZnO is reduced.

The crystallite size (D) of the films prepared with different percentages of SnO$_2$ was calculated from the more intense peak using the Scherrer formula[51]:

$$D = \frac{0.9 \times \lambda}{\beta \cos(\theta)} \qquad (1)$$

Where λ = 1.5418 Å for Cu radiation, θ is the diffraction angle, and β is the full width at Half-maximum FWHM.

The crystallite size values for different percentages of SnO$_2$ are given in Table 1.

We note that the crystallite size of ZnO decreases as the percentage of tin oxide increases from 61 to 11 nm, which is attributed to the presence of SnO$_2$ that may cause an aggregation of ZnO particles. This finding is consistent with literature results reporting that the inhibition of the aggregation of ZnO increased with increasing SnO$_2$ content[52–54], and[47]. The decrease in aggregation has been reported to correlate well with higher surface areas in nanocomposite photocatalysts[55]. It was shown by Abdelkrim et al. and Tischner et al. that the SnO$_2$ films exhibit uniform morphology with small crystallites[56,57].

In addition to D, other parameters related to lattice stress and their variations have been calculated and are analyzed in detail in the support document. In addition, additional information on the elemental composition and its variation with increasing Sn content is available in the supplementary document.
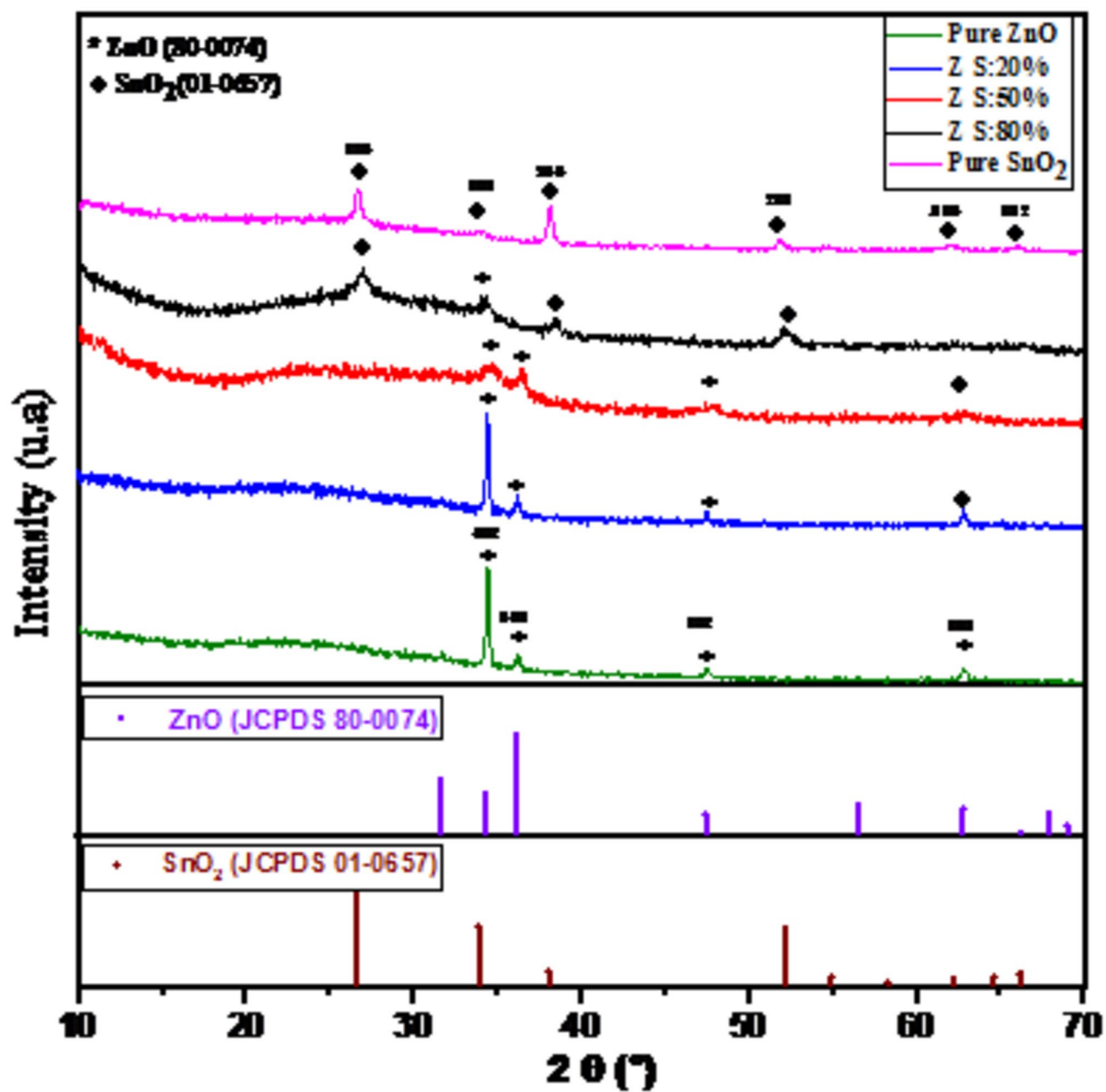
Fig. 2. XRD diffractograms of pure ZnO, pure SnO_2 and ZnO−SnO_2 (20%, 50%, 80%) thin films.

Material	Preferential orientation	D(nm)
ZnO	002 H	61
Zn:Sn(20%)	002 H	32
Zn:Sn(50%)	110 T / 002 H	11
Zn:Sn(80%)	110 T / 002 H	17
SnO_2	110 T	28

Table 1. Crystallite size of different percentages of SnO_2.

5

The impact of varying percentages of SnO_2 on the morphology of ZnO samples is illustrated through the SEM images in Fig. 3 and the AFM images in the support document.

For the pure oxides of SnO_2 and ZnO, the samples show a smooth morphology consisting of compact grains, densely packed and uniform (see Fig. 3a,b). The micrographs of the $ZnO-SnO_2$ nanocomposites with different percentages of tin oxide revealed the presence of particles with different sizes. In particular, the sample deposited with 50% percent of tin oxide exhibits small particles, indicative of a polycrystalline film[58]. As the percent of tin
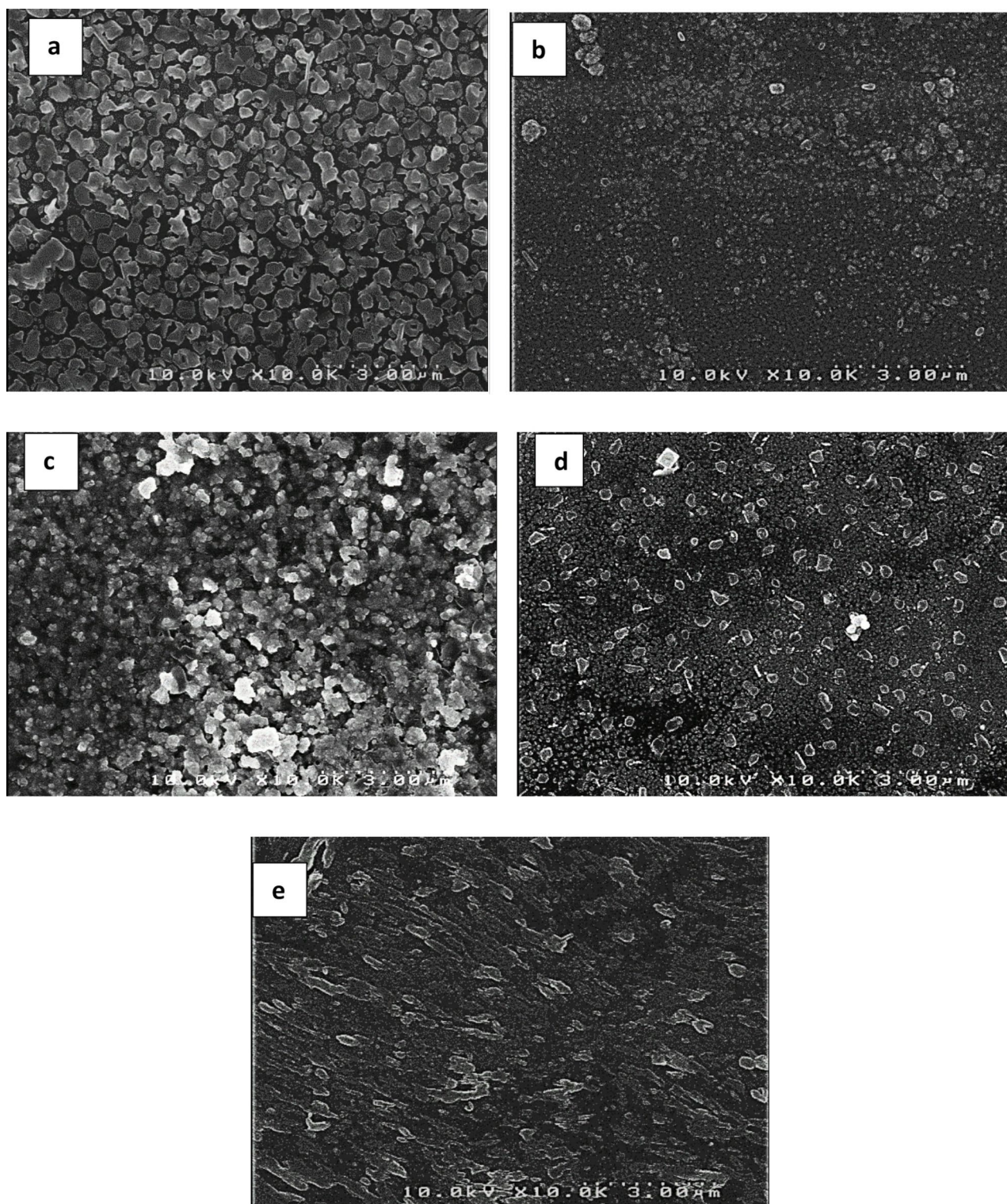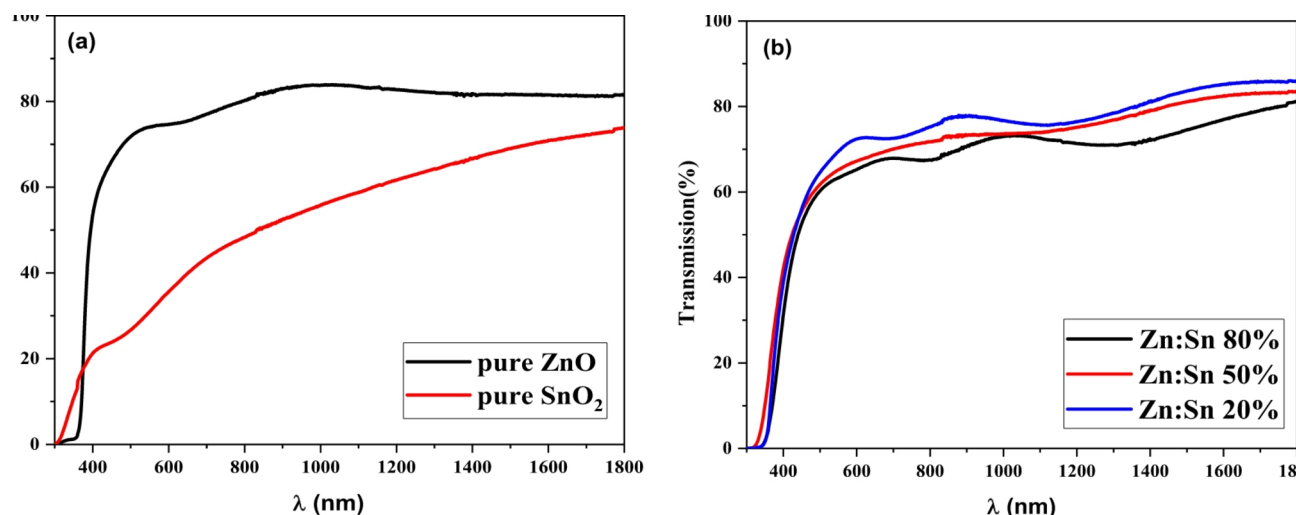

Fig. 3. SEM images of $ZnO-SnO_2$ nanocomposites synthesized by varying the percentages of SnO2: (**a**) ZnO pure, (**b**) SnO_2 pure, (**c**) $SnO_2 = 20\%$, (**d**) $SnO_2 = 50\%$ and (**e**) $SnO_2 = 80\%$.

	ZnO	SnO$_2$	Zn:Sn(20%)	Zn:Sn(50%)	Zn:Sn(80%)
d (nm)	175	326	215	360	740
Ra (nm)	108	91	111	133	143

Table 2. Thickness and roughness of nanocomposites ZnO−SnO$_2$.

Fig. 4. Transmission spectrum of Zn:Sn thin films: (**a**) pure ZnO and SnO$_2$, (**b**) Zn:Sn(20%, 50% and 80%).

oxide increases to 80% (Fig. 3e), the samples consisted of aggregates of particles. This can be explained by the presence of the two phases of tin and zinc oxides.

Besides, the film thicknesses were estimated by measuring the cross-section of the SEM images. As shown in Table 2, we can note that the thicknesses for different nanocomposites prepared were varied from 175 to 740 nm. The value of the thickness increases as the percentage of Sn increases in the samples, and the highest thickness value of about 740 nm was characteristic of the nanocomposite deposited with 80% of tin oxide.

The surface roughness of pure oxides (ZnO and SnO$_2$) and the nanocomposite ZnO−SnO$_2$ for different percentages of tin oxide were studied by Atomic force microscopy AFM. Additional details and specific surface characteristics from the AFM analysis are available in the support document.

Optical properties
Optical transmittance spectra of ZnO−SnO$_2$ thin films with different percentages of tin are presented in Fig. 4.

All the spectra exhibit an abrupt absorption edge, which is characteristic of materials with direct energy band gaps. Observing the transmission spectra of the films reveals an increased occurrence of interference fringes (oscillations), which stem from a multiple reflection phenomenon between the free surface and the substrate-contacting surface. Notably, the heightened presence of these fringes suggests a higher level of homogeneity in the films prepared with varying percentages of tin oxide compared to the pure thin films of ZnO and SnO$_2$. From Fig. 4a, we can note that the pure thin film of ZnO present a higher transmission value than the pure SnO$_2$.

In the transmission spectra of ZnO−SnO$_2$ nanocomposites with different percentage of Sn (Fig. 4b), it is evident that the transmittance decreases from 80% to around 70% with the increasing percentage content of Sn in the visible region. The sample Zn:Sn(80%) presents the lower transmission value of about 70%.

To obtain a deeper understanding of the photocatalytic properties exhibited by the ZnO series, it is essential to elucidate the energy band structure and transport characteristics of the heterogeneous semiconductor. This is crucial, as only the photo-excited charge carriers reaching the surface contribute to the generation of reactive species responsible for the degradation of dye molecules[59]. The optical band gap energy (E_g) is determined using the following relation[60]:

$$(\alpha h\upsilon)^n = A(h\upsilon - E_g) \tag{2}$$

Where α is the absorption coefficient, hυ is the photon energy, A is a constant, and $n = 2$ for an indirect allowed transition and $n = 1/2$ for a direct allowed transition.

Figure 5 shows the variation of $(\alpha h\upsilon)^2$ versus hυ. The Eg values of band gap energy are determined by plotting $(\alpha h\upsilon)^2$ versus (hυ) and by extrapolating the linear part of the curve until its intercept with the photon energy axis (Fig. 5).

In Table 3, the optical band gap values (E_g) of ZnO−SnO$_2$ nanocomposites with different tin content are shown. We can see that the values of the optical band gap of pure oxides ZnO and SnO$_2$ thin films are 3.29 and 3.71 eV, respectively. From the literature, the measured optical band gaps of ZnO thin films are reported to lie in
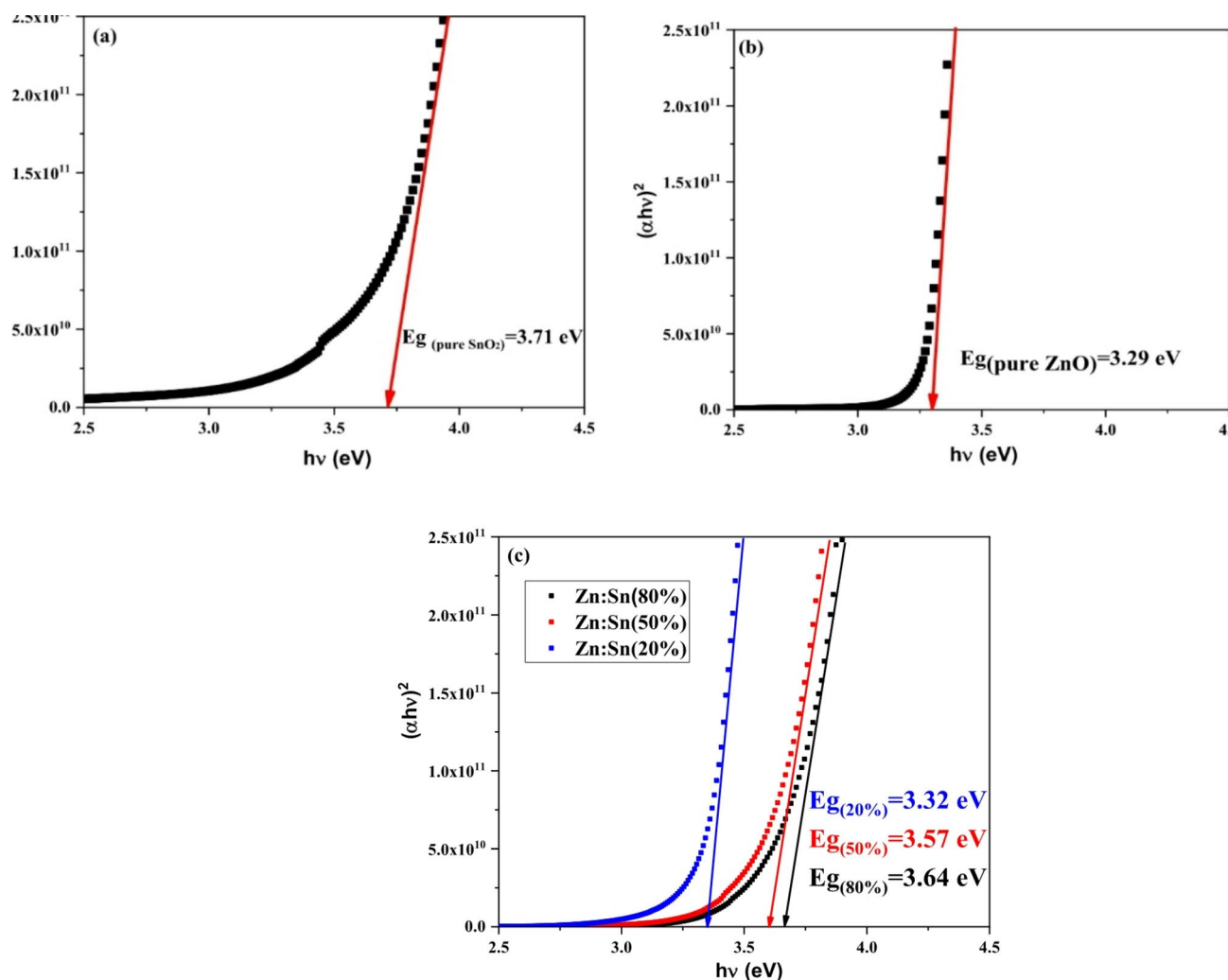
Fig. 5. $(\alpha h\nu)^2$ versus $h\nu$ plots of ZnO−SnO$_2$ thin films for different content of tin oxide: (**a**) Pure SnO$_2$, (**b**) Pure ZnO, and (**c**) Zn:Sn(20%, 50% and 80%).

Samples	Pure ZnO	ZnO−SnO$_2$ (20%)	ZnO−SnO$_2$ (50%)	ZnO−SnO$_2$ (80%)	Pure SnO$_2$
Eg (eV)	3.29	3.32	3.57	3.64	3.71
E$_u$ (eV)	–	0.69	0.39	0.26	–

Table 3. Optical properties of ZnO−SnO$_2$ thin films for different content of Tin.

the range (3.2–3.4 eV), and those of SnO$_2$ thin films are reported to lie in the range (3.72–3.83 eV). Thus, we can notice that our band gaps are in agreement with those reported previously[61,62].

For ZnO−SnO$_2$ nanocomposites prepared with different content of SnO$_2$ (Fig. 5c), the values of the optical band gap vary from 3.32 to 3.64 eV. We can observe that the bandgap energy increases with the increase of the tin content.

These relative shifts of values of band gap energy may be due to the influence of several factors such as structural parameters and lattice strain; these results confirm those discussed in the XRD results.

The band gap is related to the appearance of band tails in material band diagrams. In this context, the Urbach energy (Eu) is estimated from the inverse slope of the linear plot between Ln(α) and $h\nu$ (Fig. 6). The Urbach tail values are given in Table 3. It is evident that the Urbach energy decreases with the increase in tin content. Accordingly, the Urbach and the bandgap energy are inversely correlated.

Photocatalytic activity
The photo-catalytic degradation of MB was studied using ZnO−SnO$_2$ nanocomposites for different percentages of tin as photocatalysts. The organic dye presents a strong absorbance band at 660 nm. Its intensity decreases when MB degrades, and this variation in the intensity was assessed at regular time intervals.
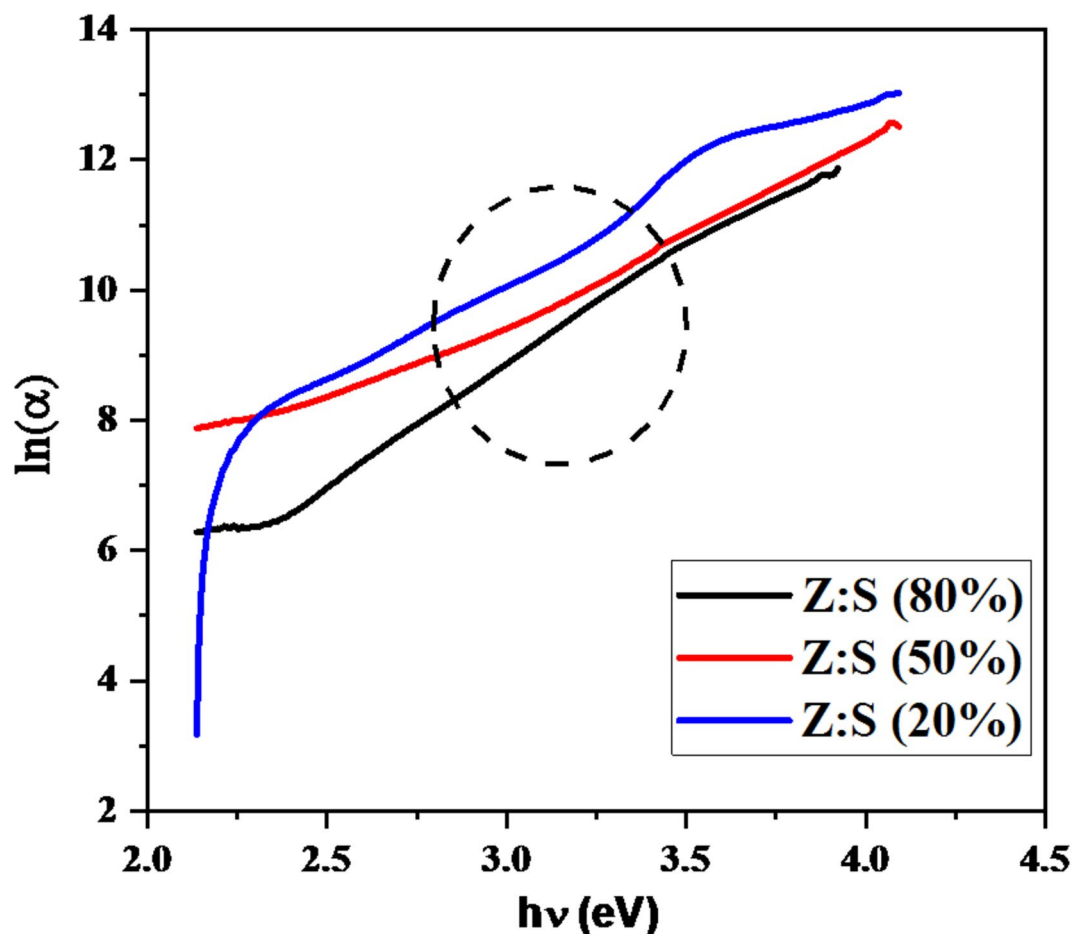
Fig. 6. Variation of Ln(α) with photon energy of ZnO−SnO₂ thin films for different percentage of tin oxide (20%, 50% and 80%).

The use of UV light in our experiments can be justified by both intrinsic properties of the SnO_2–ZnO composite and environmental conditions of Tunisia. SnO_2 and ZnO have a wide bandgap around 3.37 and 3.2 eV, respectively, showing that they are mainly sensitive under UV light. This high-energy UV radiation promotes better generation of electron-hole pairs and catalytic activity. Since UV and visible light are able to activate the composite, we preferred the use of UV light because it can bring more reliable activation for such high bandgap material. Natural UV radiation in Tunisia's summer climate is rich, which makes it a practical and effective choice since the solar irradiance intensity and UV radiation comprise approximately 3–5% of the total sunlight. Due to this fact, UV light was chosen to ensure superior photocatalytic performance that will go hand in hand with the material properties and also depend on the local environmental conditions.

Figure 7 shows the degradation rate of MB after UV irradiation as a function of time achieved with ZnO–SnO_2 thin films having different percentages of tin.

The photocatalytic degradation rate was determined using the following relation[63]:

$$\text{photodegradation rate \%} = \frac{A_0 - A}{A_0} \times 100 \tag{3}$$

Where A_0 is the initial absorbance of the dye solution and A is the absorbance after UV irradiation.

According to Fig. 7, all samples showed higher photocatalytic activity than the two pure oxides. This proves that the simultaneous presence of two phases resulted in a synergistic effect and improved the photocatalytic activity.

As we can see, the photocatalytic efficiency increases with the increase in the percentage of tin. Indeed, the sample ZnO–SnO_2 with 80% tin exhibited the highest photocatalytic activity among the composites tested. MB degradation efficiency with Zn:Sn(80%) reached 91% after 180 min of UV irradiation, as shown in Fig. 6, and was 51% higher than that achieved with pure ZnO.

This increase in photocatalytic activity with the increase in the percentage of tin oxide can be explained by the simultaneous presence of semiconductors possessing different energy levels of their corresponding conduction and valence bands[64]. Besides, the generation of electron-hole pairs under UV light irradiation, which constitutes the fundamental basis of the degradation process, is influenced by multiple factors, including particle size
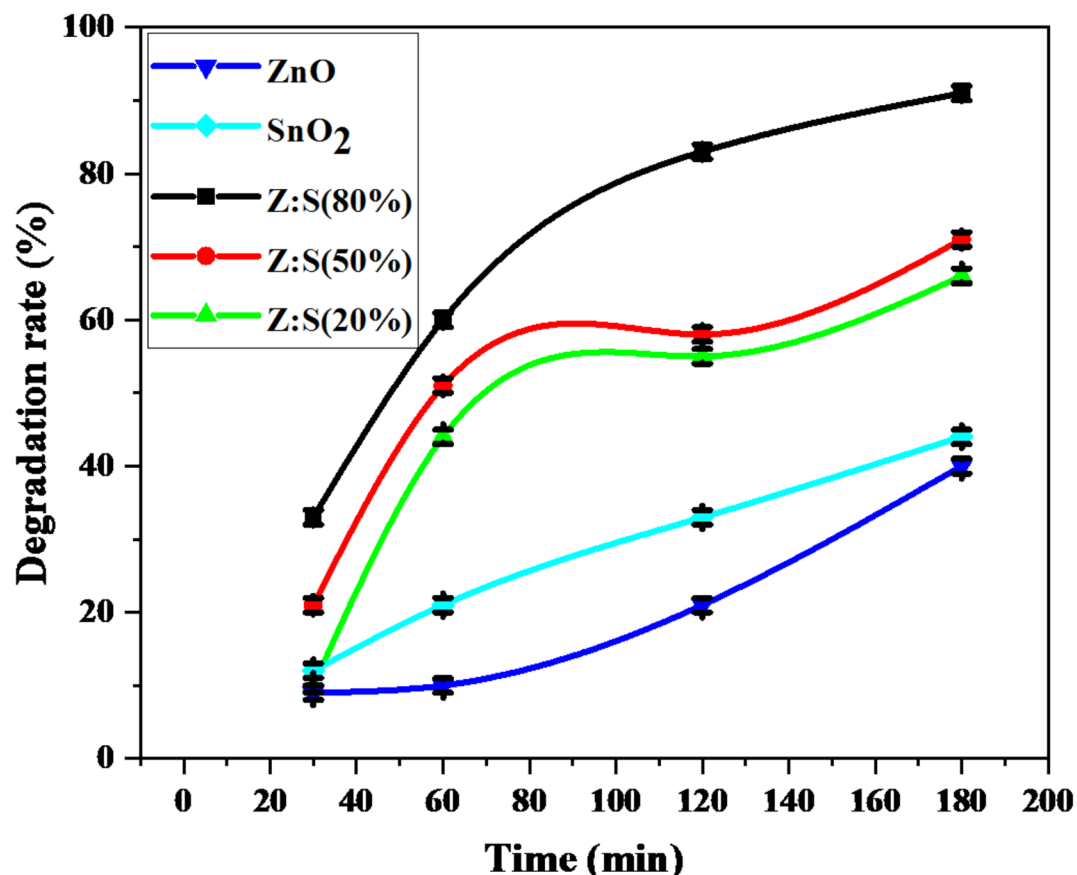
Fig. 7. Degradation rate of MB after UV irradiation as a function of time for pure ZnO, pure SnO$_2$ and for ZnO–SnO$_2$ thin films having different percentages of tin.

decrease, morphology, bandgap energy, and the formation of hetero-junction composites. Consequently, the observed enhanced photodegradation rate in 80% SnO$_2$ films may be attributed their favorable crystallinity, which results in a higher yield of electron-hole pairs.

Indeed, the structural and morphological results prove this enhancement, and the sample prepared with 80% of tin oxide exhibits the highest surface roughness (RMS) and the small crystallite size leading to an increase in the adsorption of the MB on the surface. These parameters facilitate the separation and the transfer of photogenerated charge carriers, resulting in an enhancement of photocatalytic efficiency.

Moreover, it can be observed from Fig. 8, that the degradation rate increases as the irradiation time increase. This indicates that the highest degradation of MB was obtained after 3 h of UV irradiation.

Figure 9a, shows the variation of ln (A$_0$/A) versus irradiation time for the two pure oxides and the samples of Zn:Sn for different content of tin (20, 50 and 80%).

All curves exhibited good linear correlation. This result proved that the photodegradation of MB with Zn:Sn catalysts followed pseudo-first-order kinetics[65]:

$$\ln \left(\frac{A_0}{A} \right) = Kt \tag{4}$$

Where A$_0$ is the initial absorbance of the MB dye, A is the absorbance of the MB dye after irradiation time 't' and K is the degradation rate constant.

The constants rate kinetics, K, were calculated from the slope of ln(A$_0$/A) versus irradiation time (t) as shown in Fig. 9b.

It can be seen that the value of the rate constant increases when the percentage of tin increases, which proves that the presence of two phases, ZnO and SnO$_2$ enhances the photocatalytic performance under ultra-violet light. Moreover, the Zn:Sn(80%) exhibited the highest reaction rate constant (K) and hence the highest photocatalytic activity.

To evaluate the photocatalytic stability of the Zn:Sn(80%) sample, five consecutive cycles of MB degradation under UV light were performed (Fig. 10). A cleaning protocol of the surface was used before each cycle to ensure a reliable film recovery. Particularly, the active layer was rinsed several times with distilled water. As a result, a negligible decrease in the photocatalytic efficiency was observed after five cycles, demonstrating the outstanding
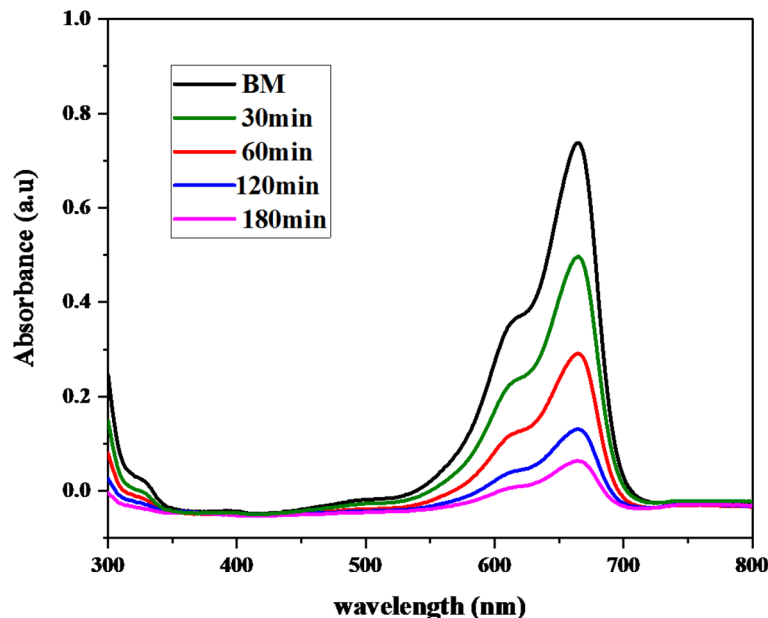
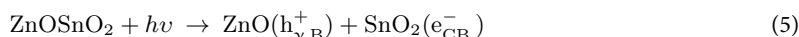**Fig. 8.** UV–vis spectra of the MB solutions at different irradiation times.

stability of Zn:Sn(80%) thin films for degrading MB. From this knowable, ZnO−SnO$_2$ (80%) sample possessed outstanding photocatalytic activity and stability.

As shown by the XRD and AFM results, the Zn:Sn(80%) present the small crystallinity size and the higher roughness. This result justifies the enhanced photoactivity of the coupled ZnO−SnO$_2$ samples.

The proposed dye degradation mechanism in the presence of ZnO−SnO$_2$ thin film is schematically detailed in Fig. 11.

It is well-known that hydroxyl radicals remove the organic contaminants from wastewater on the surface of the ZnO−SnO$_2$ thin films. In fact, under irradiation, absorption of an efficient photon by ZnO−SnO$_2$ produces a generation of electron-hole pairs. These charge carriers reach the surface of the catalyst; the generated electrons are absorbed by O$_2$ molecules to form the radical anion of oxygen O$_2^{-\cdot}$, while the holes are trapped by surface-bound H$_2$O to create hydroxyl radicals OH$^\cdot$. The formed radicals (O$_2^{-\cdot}$ and OH$^\cdot$) are useful species for the degradation of the organic MB dyes.

The dye degradation mechanism of ZnO−SnO$_2$ thin films can be described as follows:

$$ZnOSnO_2 + h\upsilon \; \rightarrow \; ZnO(h_{\upsilon B}^+) + SnO_2(e_{CB}^-) \tag{5}$$

$$O_2 + e_{CB}^- \; \rightarrow \; O_2^{-\cdot} \tag{6}$$

$$H_2O + h_{\upsilon B}^+ \; \rightarrow \; H^+ + OH^\cdot \tag{7}$$

$$MB_{dye} + OH^\cdot \; \rightarrow \; CO_2 + H_2O \tag{8}$$

The electrons within the conduction band of SnO$_2$ interact with molecular oxygen adsorbed onto the SnO$_2$ surface, leading to the formation of superoxide radical anions (O$_2^{-\cdot}$) Eq. (6). These O$_2^{-\cdot}$ radicals subsequently engage with H$_2$O, resulting in the creation of OH$^\cdot$ radicals. Conversely, the holes that migrate to ZnO react with hydroxyl groups attached to the surface (or with H$_2$O), generating hydroxyl radical species (OH$^\cdot$) as shown in Eq. (7). These OH$^\cdot$ radicals act as highly effective oxidants, enabling the mineralization of organic compounds like MB into degradation by-products such as H$_2$O and CO$_2$ Eq. (8).

This study presents an effective approach to boost the photocatalytic efficiency of SnO$_2$ thin films by integrating varying concentrations of Sn particles into the lattice of ZnO. This incorporation results in a heightened band gap within semiconductors, which proves advantageous for enhancing photocatalytic activity. A widened band gap signifies the semiconductor's capability to absorb photons with greater energy (shorter wavelengths), encompassing a broader spectrum of solar radiation. This expanded absorption range augments light absorption efficiency, consequently elevating photocatalytic performance. Moreover, the adoption of the spray pyrolysis technique, deemed most suitable for thin film fabrication in photocatalytic applications, was deliberate to augment degradation kinetics owing to its structured morphology. Porous thin films, a hallmark in photocatalysis, offer increased surface area, thus optimizing active sites for reactions and amplifying efficiency. Their porous architecture facilitates efficient mass transfer kinetics while minimizing charge carrier recombination, thereby ensuring sustained activity and stability. Versatile and cost-effective, such films hold immense potential for diverse applications like water splitting and pollutant degradation, propelling advancements in photocatalytic technologies.
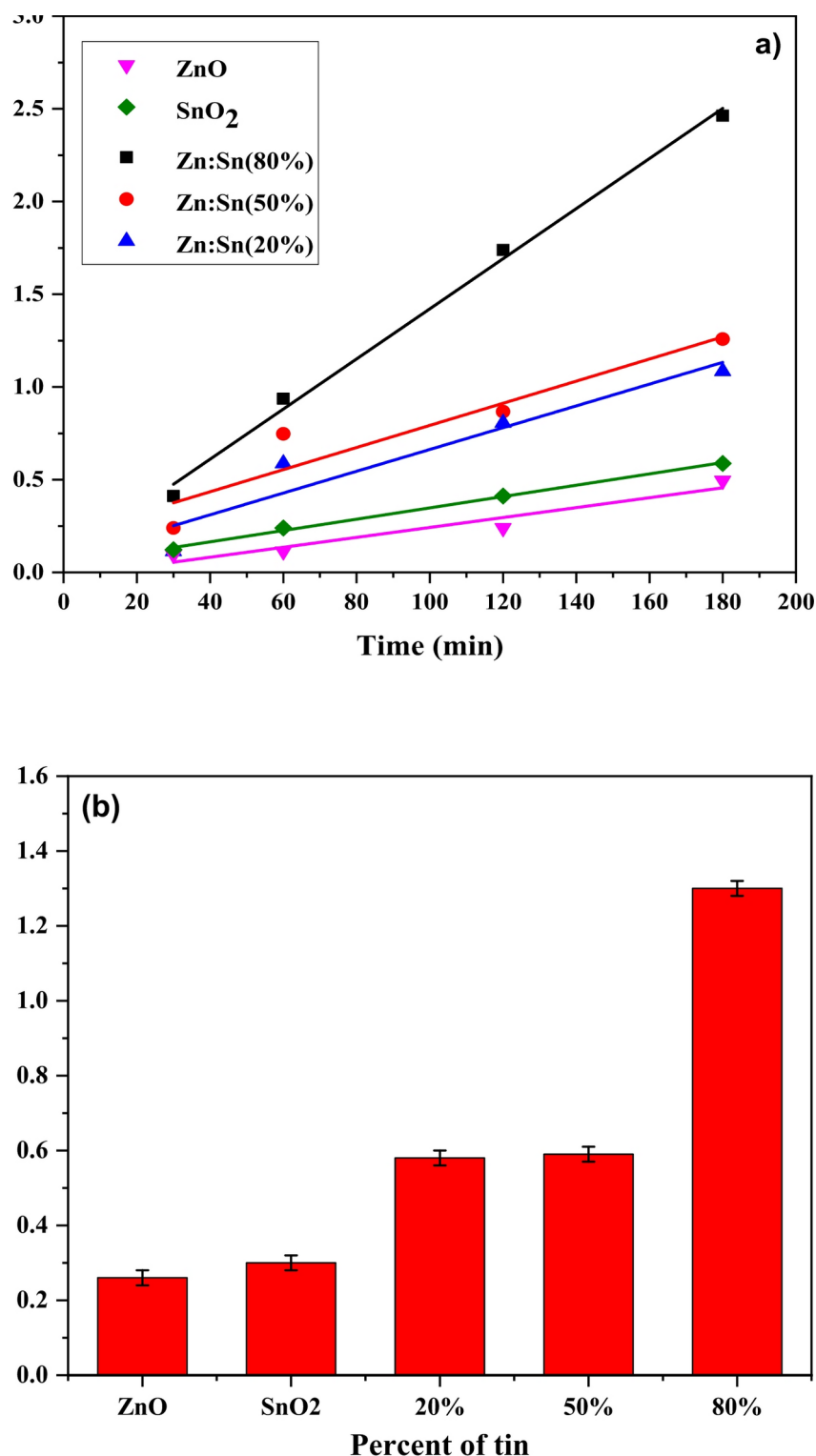
Fig. 9. (**a**) Photocatalytic degradation kinetics of MB dyes versus irradiation time. (**b**) The kinetic rate K as a function of tin content.

The comparison of our study to previous works highlights several key benefits these works are gathered with their main results in the Table 4, demonstrating the efficacy of our approach. The UV spray pyrolysis method achieved 91% degradation within 180 min, showing high repeatability compared to other methods with additional activation processes. For example, Zarei et al.[66] reported a degradation rate of 70% in 240 min under UV light, while Dharmana et al.[44] obtained 82.45% in 120 min under visible light. However, neither demonstrated the same stability or repeatability as our study. Our material exhibited excellent stability with
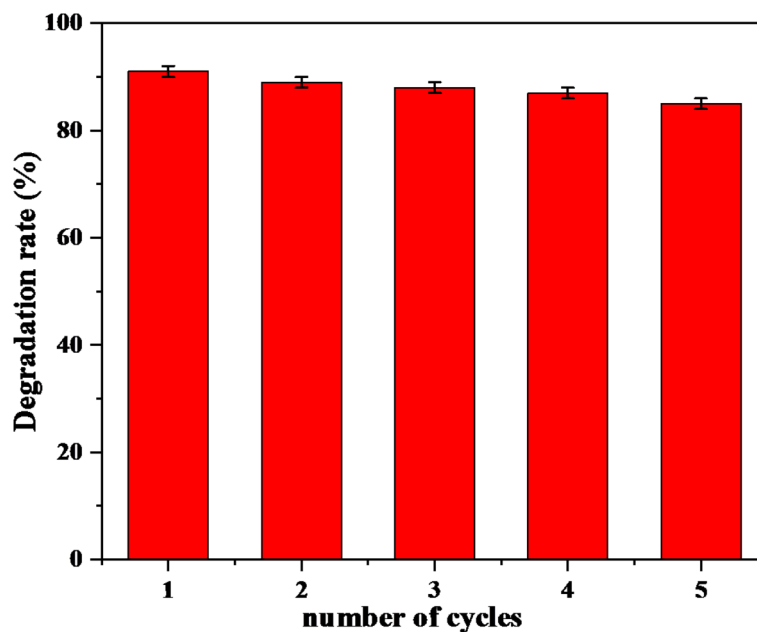
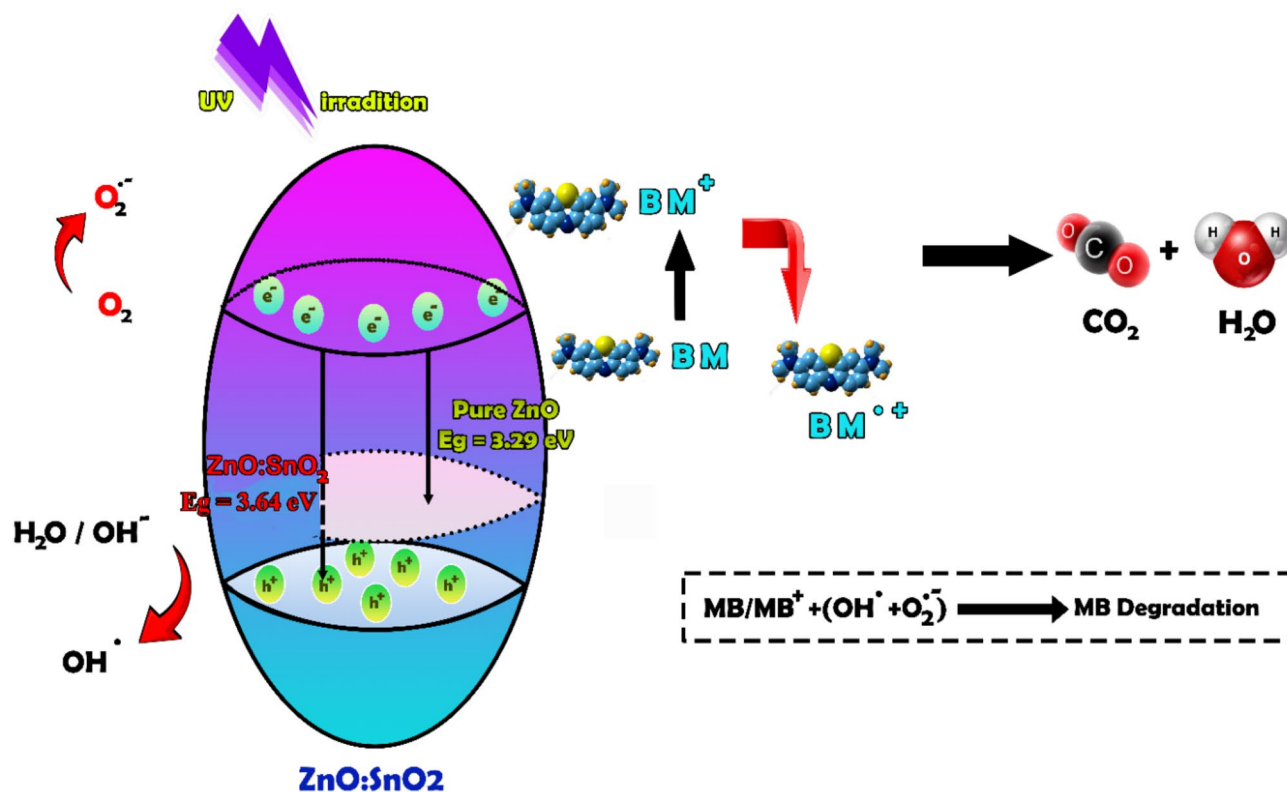**Fig. 10**. Recyclability of Zn:Sn(80%).

Fig. 11. Dye degradation mechanism for the ZnO−SnO$_2$ nanocomposite.

less than 10% efficiency decay over six cycles, making it durable for regular use. Furthermore, other studies, such as Shama et al.[69], showed lower degradation efficiency (only 55% in 125 min) compared to our material. Kumaravelan et al.[70] demonstrated 90% degradation in just 90 min but did not assess repeatability over multiple cycles. In contrast, our method ensures both rapid degradation and long-term stability. Therefore, our approach provides a competitive and practical strategy with superior photocatalytic performance, reproducibility, and stability compared to previously demonstrated techniques.

Study	Synthesis method	Light source	Degradation efficiency	Key advantages	Reproductibilty	References
Our study	Spray pyrolysis	UV light	91% in 180 min Improved over single oxides	Porous surface Higher degradation rate in less time with high repeatability and stability	Less than 10% efficiency loss in 6 cycles repeatability	This work
S. Zarei, et al. (2022)	Sol–gel spin coating	Ultraviolet irradiation	70% in 240 min	Lower recombination rate of electron hole pairs, improved efficiency	Not studied	66
I. Riahi et al. (2021)	Sputtering	Visible light	66% in 210 min	Cost-effective, high surface area for better catalytic activity	Not studied	67
Dharmana et al. (2024)	Hydrothermal	Visible light	82.45% in 120 min	Excellent surface uniformity enhanced catalytic activity	High stability 81% degradation rate after 3 cycles	44
T Martínez et al.	Dip-coating method	UV light	88% in 180 min	Good photocatalytic performance with higher rough surfaces	Not studied	68
Shama S et al. (2019)	Electrodepositon method	UV light	55% in 125 min	High stability, effective charge separation , low degradation	Degradation decreases less than 5% after 5 cycles	69
Kumaravelan et al. (2021)	Spray pyrolysis	UV–visible irradiation	90% in 90 min	Improved photocatalytic activity, high degradation in a short time	Not studied	70

Table 4. Comparison of photocatalytic degradation efficiency and key advantages of different synthesis methods for SnO_2–ZnO-based materials.

Conclusions

In this paper, ZnO–SnO_2 nanocomposites with different percentages of tin oxide (20, 50 and 80%) were deposited by spray pyrolysis while their photocatalytic activity was studied by photodegradation of MB as an organic pollutant under UV light irradiation.

The properties of the ZnO elaborated thin films were optimized by the incorporation SnO_2 nanoparticles that was proved by different material characterisation techniques. The crystalline quality and phase composition of ZnO–SnO_2 films were investigated revealing high purity and lower crystallite size for the higher Sn samples. The morphology of ZnO–SnO_2 nanocomposites varies with SnO_2 content, transitioning from compact grains in pure oxides to particle aggregation at higher SnO_2 percentages, reflecting the coexistence of tin and zinc oxide phases. Thickness and Roughness increases with the increase of Sn percentage. The optical transmittance and band gap of ZnO–SnO_2 thin films vary with SnO_2 content, showing increased homogeneity, reduced transmittance, and a rising band gap with higher tin oxide percentages, consistent with structural changes and lattice strain.

The dye degradation for the pure ZnO was found to be 40% and increased up to 91% for ZnO–SnO_2 (80%). This is the highest efficiency achieved all over the samples. Moreover, the Zn:Sn(80%) nanocomposite verified the high photocatalytic activity after being recycled for five MB degradation cycles.

The enhanced photoactivity was attributed to the increased charge separation resulting from the coupling of ZnO and SnO_2 semiconductors with different energy levels of their conduction and valence bands. The higher roughness and the small crystallinity size are important factors to enhance the photocatalytic efficiency of the samples.

Consequently, the ZnO–SnO_2 nanocomposite is a promising candidate in the treatment of industrial wastewater to reduce organic pollutants.

Further studies are needed to verify the stability of the films after the photocatalytic process by analyzing their structural and morphological properties. Additionally, the optimized sample could achieve higher degradation efficiency and stability by being decorated with 2D materials, such as graphene oxide. This will be the subject of future research.

Data availability
Data can be obtained from the corresponding authors upon reasonable request.

References
1. Rahman, T. et al. Progress in plasma-based doping semiconductor photocatalysts for efficient pollutant remediation and hydrogen generation. *Sep. Purif. Technol.* **320**, 124141 (2023).
2. Molleman, B. et al. Evaluation of the applicability of a metal oxide semiconductor gas sensor for methane emissions from agriculture. *Inform. Process. Agric.* **11**(4), 573–580 (2023).
3. Siebentritt, S. Chalcopyrite compound semiconductors for thin film solar cells. *Curr. Opin. Green. Sustainable Chem.* **4**, 1–7 (2017).
4. Hao, Q. et al. Bandgap engineering of high mobility two-dimensional semiconductors toward optoelectronic devices. *J. Materiomics.* **9** (3), 527–540 (2023).
5. Kumar, Y. & Shishodia, M. S. Transparent conducting oxides (TCOs) based gratings for light absorption in near infrared spectrum. *Results Opt.* **13**, 100542 (2023).
6. Saxena, N. et al. Effect of the triple (Al, Ga, In) doping in ZnO nanostructures on its transmission, conductivity, and stability for TCO applications. *Mater. Lett.* **306**, 130886 (2022).
7. Satılmış, H. et al. Cd-supported CuO-ZnO binary oxide thin films: Synthesis, microstructural, and optoelectronic properties. *Opt. Mater.* **148**, 114851 (2024).

8. Ahmad, M. et al. Phytogenic fabrication of ZnO and gold decorated ZnO nanoparticles for photocatalytic degradation of Rhodamine B. *J. Environ. Chem. Eng.* **9** (1), 104725 (2021).

9. Dutta, S. et al. Contamination of textile dyes in aquatic environment: Adverse impacts on aquatic ecosystem and human health, and its management using bioremediation. *J. Environ. Manage.* **353**, 120103 (2024).

10. Sharma, J., Sharma, S. & Soni, V. Classification and impact of synthetic textile dyes on aquatic flora: A review. *Reg. Stud. Mar. Sci.* **45**, 101802 (2021).

11. Banyal, R. et al. Construction of novel BiOI/CuInS2/ZnO Dual S-scheme charge transfer pathway for efficient antibiotic degradation. *J. Phys. Chem. Solids* **195**, 112132 (2024).

12. Chnadel, N. et al. Z-scheme photocatalytic dye degradation on AgBr/Zn (Co) Fe2O4 photocatalysts supported on nitrogen-doped graphene. *Mater. Today Sustain.* **9**, 100043 (2020).

13. Aziz, K. H. et al. Recent advances in water falling film reactor designs for the removal of organic pollutants by advanced oxidation processes: A review. *Water Resour. Ind.* **30**, 100227. (2023).

14. Soni, V. et al. Visible-light-driven photodegradation of methylene blue and doxycycline hydrochloride by waste-based S-scheme heterojunction photocatalyst Bi5O7I/PCN/tea waste biochar. *Chemosphere* **347**, 140694. (2024).

15. Mohod, A. V. et al. Degradation of rhodamine dyes by advanced oxidation processes (AOPs)–focus on caviation and photocatalysis-A critical review. *Water Resour. Ind.* **30**, 100220 (2023).

16. Pathania, D. et al. Exploring phytochemical composition, photocatalytic, antibacterial, and antifungal efficacies of Au NPs supported by Cymbopogon flexuosus essential oil. *Sci. Rep.* **12** (1), 14249 (2022).

17. Azhar, M. *Historical Overview and Future Prospects of Photocatalysis. Graphene-Based Photocatalysts: from Fundamentals To Applications* 47–65 (Springer Nature Switzerland, 2024).

18. Algarni, T. et al. Green synthesis of mixed ZnO–SnO2 nanoparticles for Solar-Assisted degradation of synthetic dyes. *Catalysts* **13** (12), 1509 (2023).

19. Hamrouni, A. et al. Sol-gel synthesis and photocatalytic activity of ZnO–SnO$_2$ nanocomposites. *J. Mol. Catal. A: Chem.* **390**, 133–141 (2014).

20. Zhenya, S., Yundi, D. & Weiying, Z. Structure and property investigation of composite ZnO/SnO2 nanocrystalline particles after high-pressure treatment. *J. Nanomaterials* **2008**(1), 286069 (2008).

21. Lv, T., Pan, L., Liu, X. & Sun, Z. Enhanced photocatalytic degradation of methylene blue by ZnO–reduced graphene oxide–carbon nanotube composites synthesized via microwave-assisted reaction. *Catal. Sci. AndTechnology.* **2** (11), 2297 (2012).

22. Pathania, D. et al. Essential oil-mediated biocompatible magnesium nanoparticles with enhanced antibacterial, antifungal, and photocatalytic efficacies. *Sci. Rep.* **12** (1), 11431 (2022).

23. Ameur, I. et al. Influence of magnesium doping on microstructure, optical and photocatalytic activity of zinc oxide thin films synthesis by sol–gel route. *Appl. Phys. A.* **127**, 1–14 (2021).

24. : Kim, Sungjin, et al. Highly porous SnO2/TiO2 heterojunction thin-film photocatalyst using gas-flow thermal evaporation and atomic layer deposition. *Catalysts* 11.10 : 1144. (2021).

25. Widyastuti, E. et al. Photocatalytic antimicrobial and photostability studies of TiO2/ZnO thin films. *Arab. J. Chem.* **16**, 105010 (2023).

26. Cruz, M. R. et al. Development of SnO2–ZnO thin films as a photocatalyst for obtaining alternative fuels through photocatalytic reactions. *Solid State Sci.* **137**, 107112 (2023).

27. Kulis-Kapuscinska, A. et al. Photocatalytic degradation of methylene blue at nanostructured ZnO thin films. *Nanotechnology* **34**, 155702 (2023).

28. Erfan, N. A. et al. Synergistic doping with Ag, CdO, and ZnO to overcome electron-hole recombination in TiO$_2$ photocatalysis for effective water photo splitting reaction. *Front. Chem.* **11** 1301172 (2023).

29. Deng, Y. et al. Improving separation efficiency of photogenerated charges through combination of conductive polythiophene for selective production of CH4. *Catalysts* **13**(7), 1142 (2023).

30. Vinayagam, V. et al. Recent developments on advanced oxidation processes for degradation of pollutants from wastewater with focus on antibiotics and organic dyes. *Environ. Res.* **240**, 117500. (2023).

31. Shifu, C., Wei, Z., Wei, L. & Sujuan, Z. Preparation, characterization and activity evaluation of p–n junction photocatalyst p-ZnO/n-TiO2. *Appl. Surf. Sci.* **255**, 2478–2484 (2008).

32. Sakthivel, S., Geissen, S. U., Bahnemann, D. W., Murugesan, V. & Vogelpohl, A. *J. Photochem. Photobiol A: Chem.* **148** 283–293. (2002).

33. Nadikatla, S. et al. Review of recent developments in the fabrication of ZnO/CdS heterostructure photocatalysts for degradation of organic pollutants and hydrogen production. *Molecules* **28**(11), 4277 (2023).

34. Zhang, X. et al. Nanocellulose/carbon Dots hydrogel as superior intensifier of ZnO/AgBr nanocomposite with adsorption and photocatalysis synergy for cr (VI) removal. *Int. J. Biol. Macromol.* **233**, 123566 (2023).

35. Yang, L. et al. Energy band management of corn-like ZnO/Ag2S heterojunctions for efficient light harvesting and enhanced photocatalysis. *J. Chem. Phys.* **161**, 13 (2024).

36. Gawade, V. V. et al. Biogenic fabrication of ZnO–SnO2 nanocomposite for effective photodegradation of toxic industrial dyes. *Res. Chem. Intermed.* **50** (1), 323–338 (2024).

37. Li, F. et al. Fabrication of ZnO–SnO2 heterojunction inverse opal photonic balls for chemiresistive acetone sensing. *Sens. Actuators B.* **400**, 134887 (2024).

38. Salda na-Ramírez, A., Alfaro Cruz, M. R., Ju´arez-Ramírez, I. & Torres-Martínez, L. M. Influence of the power density and working pressure in the Magnetron co-sputtering deposition of ZnO–SnO2 thin films and their effect in photocatalytic hydrogen production. *Opt. Mater.* **110**, 11050 (2020).

39. Shabna, S. et al. Photocatalytic degradation of crystal Violet using SnO2/ZnO nanocomposite synthesized by facile sol-gel method. *J. Cluster Sci.* **35** (2), 597–606 (2024).

40. Lamba, R., Umar, A., Mehta, S. K. & Kansal, S. K. ZnO doped SnO2 nanoparticles heterojunction photo-catalyst for environmental remediation. *Alloys Compdounds.* **653**, 327–333 (2015).

41. Khodami, Z. & Nezamzadeh-Ejhieh, A. Investigation of photocatalytic effect of ZnO–SnO2/nano clinoptilolite system in the photodegradation of aqueous mixture of 4-methylbenzoic acid/2-chloro-5-nitrobenzoic acid. *Mol. Catal. A: Chem.* **409**, 59–68 (2015).

42. Begum, S., Mishra, S. R. & Ahmaruzzaman, M. Fabrication of ZnO–SnO2 nanocomposite and its photocatalytic activity for enhanced degradation of Biebrich Scarlet. *Environ. Sci. Pollut. Res.* **29**, 87347–87360 (2022).

43. Venkatesh, D. et al. Synthesis of SnO2-ZnO heterojunction composites for effective degradation of methylene blue and chromium (VI) under solar light irradiation. *Ionics* **30**, 7323–7336 (2024).

44. Dharmana, G. et al. Enhanced photo-catalytic degradation of MB dye over hydrothermal grown-up of ZnO/SnO2 catalyst. *J. Chem.* **2024**(1), 9135923 (2024).

45. MinLee, S., HeeJoo, Y. & IlKim, C. Influences of film thickness and annealing temperature on properties of sol–gel derived ZnO–SnO2 nanocomposite thin film. *Appl. Surf. Sci.* **320**, 494–501 (2014).

46. Guerram, A. et al. Synergistic performance of ZnO/SnO2 nanocomposites: Synthesis, characterization, and applications in photocatalysis and superoxide radical scavenger. *J. Cluster Sci.* **35**(7), 2231–2242 (2024).

47. Prabakaran, K. et al. Synthesis of zinc oxide and Tin oxide (ZnO/SnO2) nanocomposite for photoanode applications in dye sensitized solar cell. *J. Mater. Sci.: Mater. Electron.* **35** (30), 1–10 (2024).

48. Lai, T., Fang, T., Hsiao, Y. & Chan, C. Characteristics of Au-doped SnO2–ZnO heteronanostructures for gas sensing applications. *Vacuum* **166**, 155–161 (2019).
49. Zhao, B. et al. Atomic layer deposition of ZnO–SnO2 composite thin film: the influence of structure, composition and crystallinity on lithium-ion battery performance. *Electrochim. Acta.* **320**, 134604 (2019).
50. Lee, S. H. et al. Effects of thermal annealing time and molar ratio of channel layers on solution-processed ZnO/SnO2 thin-film transistors. *Solid State Electron.* **165**, 107765 (2020).
51. Mezyen, M. et al. Visible light activated SnO 2: Dy thin films for the photocatalytic degradation of methylene blue. *RSC Adv.* **13**, 31151–31166 (2023).
52. Evstropiev, S. K. et al. Bactericidal properties of ZnO–SnO2 nanocomposites prepared by polymer-salt method. *Mater. Sci. Engineering: B.* **264**, 114877 (2021).
53. Wang, C. et al. *J. Photochem. Photobiol A: Chem.* **168** 47–52. (2004).
54. Fu, Y. et al. Enhanced property of flexible UV photodetectors based on electrospinning ZnO–SnO2 heterojunction nanofibers by the formation of Zn2SnO4. *Ceram. Int.* **49** (7), 11402–11410 (2023).
55. Caglar, B. et al. Bi2S3 nanorods decorated on bentonite nanocomposite for enhanced visible-light-driven photocatalytic performance towards degradation of organic dyes. *J. Alloys Compd.* **885**, 160964 (2021).
56. Tischner, A., Maier, T., Stepper, C. & Köck, A. Ultrathin SnO2 gas sensors fabricated by spray pyrolysis for the detection of humidity and carbon monoxide. *Sens. Actua B: Chem.* **134**, 796–802 (2008).
57. Abdelkrim, A., Rahmanea, S., Abdelouahab, O., Abdelmalek, N. & Brahim, G. Effect of solution concentration on the structural, optical and electrical properties of SnO2 thin films prepared by spray pyrolysis. *Optik* **127**, 2653–2658 (2016).
58. Petrushenko, S. et al. Accelerated recrystallization of nanocrystalline films as a manifestation of the inner size effect of the diffusion coefficient. *Vacuum* **226**, 113349 (2024).
59. Li, D. et al. Junyong Kang, synthesis of ZnO/Si hierarchical nanowire arrays for photocatalyst application. *Nanoscale Res. Lett.* **12**, 10 (2017).
60. Harrathi, F. et al. Effect of the substrate temperature on the synthesis of the Cu2CoSnS4 thin films by spray pyrolysis for solar cells devices. *J. Mater. Sci.: Mater. Electron.* **34** (4), 304 (2023).
61. Kiruthiga, G., Rajni, K. S., Geethanjali, N. & Raguram, T. SnO2: Investigation of optical, structural, and electrical properties of transparent conductive oxide thin films prepared by nebulized spray pyrolysis for photovoltaic applications. *Inorg. Chem. Commun.* **145**, 109968 (2022).
62. Takwale, M. G. & C.M.Mahajan and Precursor molarity dependent growth rate, microstructural, optical and electrical properties of spray pyrolytically deposited transparent conducting ZnO thin films. *Micro Nanostruct.* **163**, 107131 (2022).
63. Hemmedi, I. et al. Influence of dysprosium-doped nanoparticles on the physico-chemical properties of spray-deposited CuO thin films for photocatalytic degradation of methylene blue. *J. Mater. Sci.: Mater. Electron.* **34** (36), 2306 (2023).
64. Faizan, M. et al. Enhanced photocatalytic degradation and synergistic effects of Tin-Doped zinc oxide nanoparticles for environmental remediation. *Mater. Sci. Engineering: B.* **308**, 117551 (2024).
65. Sin, J. C., Lam, S. M., Lee, K. T. & Mohamed, A. R. Preparation of rare earth-doped ZnO hierarchical micro/nanospheres and their enhanced photocatalytic activity under visible light irradiation. *Ceram. Int.* **40**, 5431–5440 (2014).
66. Zarei, S. et al. Photocatalytic properties of ZnO/SnO2 nanocomposite films: Role of morphology. *J. Mater. Res. Technol.* **17**, 2305–2312 (2022).
67. Riahi, I., Khalfallah, B. & Chaabouni, F. Effect of deposition time on the photocatalytic activity of sputtered mixed ZnO–SnO2 thin films under visible light irradiation. *Solid State Commun.* **340**, 114487 (2021).
68. Martínez, D. Y. et al. Structural, morphological, optical and photocatalytic characterization of ZnO–SnO2 thin films prepared by the sol–gel technique. *J. Photochem. Photobiol., A.* **235**, 49–55 (2012).
69. Sehar, S. et al. Superior dye degradation using SnO 2-ZnO hybrid heterostructure catalysts. *Korean J. Chem. Eng.* **36**, 56–62 (2019).
70. Kumaravelan, S. et al. Effect of Zn Dopant on SnO2 nano-pyramids for photocatalytic degradation. *Chem. Phys. Lett.* **769**, 138352 (2021).

Acknowledgements

Author contributions

S.M. and M.M. conducted the research and wrote the first draft of this manuscript. S.M. is responsible of data curation and M.M. of figure preparation. G.E.F and N.B. worked in the conceptualization, supervision and manuscript revision. E.L. was charged of supervision, manuscript editing and fund procurement.

Declarations

Competing interests

The authors declare no competing interests.

Additional information

Supplementary Information The online version contains supplementary material available at https://doi.org/10.1038/s41598-025-01370-y.

Correspondence and requests for materials should be addressed to N.B. or E.L.

Reprints and permissions information is available at www.nature.com/reprints.

Publisher's note Springer Nature remains neutral with regard to jurisdictional claims in published maps and institutional affiliations.